

Novel Au–SiO₂–WO₃ Core–Shell Composite Nanoparticles for Surface-Enhanced Raman Spectroscopy with Potential Application in Cancer Cell Imaging

Pablo Martinez Pancorbo, Kunyapat Thumavichai, Louise Clark, Tanveer A. Tabish, Jessica Mansfield, Ben Gardner, Hong Chang, Nick Stone, and Yanqiu Zhu*

With the rapid development of nanotechnology during the last decades, the ability to detect and control individual objects at the nanoscale has enabled us to deal with complex biomedical challenges. In cancer imaging, novel nanoparticles (NPs) offer promising potential to identify single cancer cells and precisely label larger areas of cancer tissues. Herein, a new class of size tunable core–shell composite (Au–SiO₂–WO₃) nanoparticles is reported. These nanoparticles display an easily improvable $\approx 10^3$ surface-enhanced Raman scattering (SERS) enhancement factor with a double Au shell for dried samples over Si wafers and several orders of magnitude for liquid samples. WO₃ core nanoparticles measuring 20–50 nm in diameter are sheathed by an intermediate 10–60 nm silica layer, produced by following the Stöber-based process and Turkevich method, followed by a 5–20 nm thick Au outer shell. By attaching 4-mercaptobenzoic acid (4-MBA) molecules as Raman reporters to the Au, high-resolution Raman maps that pinpoint the nanoparticles' location are obtained. The preliminary results confirm their advantageous SERS properties for single-molecule detection, significant cell viability after 24 h and in vitro cell imaging using coherent anti-stokes Raman scattering. The long-term objective is to measure SERS nanoparticles in vivo using near-infrared light.

the 2000s, positron emission tomography (PET) combined with computed tomography (CT) was commercialized and started to be used worldwide due to its enhanced precision in the location of areas with highly active cells compared to older techniques. Its appearance had a great impact on cancer diagnosis until today, remaining the main technique for precise tumor location in the clinical stage for most types of cancers.^[1] Unfortunately, this technique does not provide single cell detection and involves radioactive agents. More recent advances in optical imaging techniques such as deep Raman spectroscopy-based approaches have enabled the potential to find single cancer cells inside of the human body without involving ionizing radiation. These novel techniques allow higher precision via light–molecule interactions by measuring biomarkers in the microscale, such as microcalcifications in breast cancer tissue.^[2] More precise measurements using nanoscale objects

labeled with Raman reporters could achieve single cell resolution for an optimal early stage cancer detection.^[3]


In modern cancer imaging, the best personalized medical techniques are based on delivering nanoscale agents to cancer cells location while minimizing any undesirable interactions. However, many nanostructures do not arrive at the target and can induce toxicity. Hence, it is crucial to develop biocompatible nanoscale objects that contain clinically approved materials. Among many inorganic nanomaterials used, only iron-oxide (Fe₃O₄), silica (SiO₂), and gold (Au) NPs are currently clinically accepted.^[4] Iron oxide is used in imaging and thermal ablation of tumors; silica for fluorescent cancer imaging;^[5] and gold for both surface-enhanced Raman spectroscopy (SERS) and photothermal ablation of tumors.^[6] Plasmonic nanoparticles (gold or silver) coated with Raman agents provide a platform for the emission of measurable Raman signals to optically locate the nanoparticles in the body, and therefore the cancer cells too.

The combination of different materials in the same particle to perform medical diagnosis and therapy in the same agent has become an important research topic, known as theranostics. The most extensively studied composite nanoparticles

1. Introduction

Cancer is the second main cause of death globally after cardiovascular diseases, which are preventable via low-fat diet. Currently, the approach for cancer diagnosis is still based on nineteenth and twentieth century methodologies, which were supported in a limited knowledge of the cancer biology. In

P. Martinez Pancorbo, Dr. K. Thumavichai, Dr. L. Clark, Dr. T. A. Tabish, Dr. J. Mansfield, Dr. B. Gardner, Dr. H. Chang, Prof. N. Stone, Prof. Y. Zhu
College of Engineering, Mathematics and Physical Sciences
University of Exeter
Exeter EX4 4QF, UK
E-mail: Y.Zhu@exeter.ac.uk

 The ORCID identification number(s) for the author(s) of this article can be found under <https://doi.org/10.1002/adfm.201903549>.

© 2019 The Authors. Published by WILEY-VCH Verlag GmbH & Co. KGaA, Weinheim. This is an open access article under the terms of the Creative Commons Attribution License, which permits use, distribution and reproduction in any medium, provided the original work is properly cited.

DOI: 10.1002/adfm.201903549

in medical diagnosis are the colloidal ferromagnetic Fe_3O_4 wrapped by functionalized Au core-shell NP for X-rays, SERS, and MRI imaging.^[7] However, there are some important limitations in all these applications. Medium to high energy X-rays can penetrate through the soft tissue in the human body but can induce new tumors and have poor contrast between soft tissues.^[8] MRI uses Fe_3O_4 as a contrast agent due to favorable superparamagnetic properties, biodegradability, and easily modified surface properties for improved in vivo kinetics and multifunctionality.^[9] Although MRI has a penetration depth only limited by the magnetic field, it has a low contrast between bound and unbound water molecules.^[10] Further contrast is typically provided by injecting gadolinium-based enhancing agents. However, gadolinium has shown certain mechanisms for cytotoxicity.^[11] The alternative, Fe_3O_4 , is non-cytotoxic but carries the risk of magnetic aggregation, forming very large particles that will not be excreted.^[12] Au SERS uses nonionizing radiation that requires specific wavelengths in the near-infrared to penetrate the soft tissue, but penetration depth is typically up to only several centimeters.^[13] However, it is one of the few techniques that allow achieving single cancer cell detection.

On the one hand, Au NPs have been extensively used as nanoprobe for SERS cancer imaging.^[14] Their recent extension to Au nanoshells (Au NSs) covering in a core-shell structure has shown rather promising results for future biosensing,^[15] by using specific molecules with benzene rings on top as the Raman reporters.^[16] Spherical Au NPs have a range of surface plasmonic resonance wavelength excitations ranging from 510 to 572 nm for particle sizes from 3 to 100 nm, and from 520 to 932 nm excitations for Au NSs with different combinations of internal diameters and external shell thickness, respectively.^[17,18] Apparently, thinner shells and larger internal diameters of nanoshells bring redshifts in the plasmonic generation.^[18–20] Both Au NPs and Au NSs are well known for their good biocompatibility, ready bioconjugation,^[21] and optical properties via plasmons.^[22] On the other hand, Fe_3O_4 presents a behavior from superparamagnetic to ferromagnetic for 20 nm size or above of the nanoparticles which leads to significant magnetic nanoparticle aggregation.^[23,24] Therefore, there is a drive to develop new materials that integrate alternative cores for Au nanoshells core-shell nanoparticles without magnetic aggregation.

Here we have explored the use of tungsten trioxide (WO_3) that has excellent sensing properties,^[25] including unique chromic behavior activated via thermal changes, electrical currents, and gases.^[26] Additionally, some studies have previously shown potential oxygen vacancy induced ferromagnetism that brings magnetic hyperthermia capabilities,^[27,28] and both biocompatibility and antibacterial properties.^[29] Ultrasmall WO_{3-x} nanodots have also been used recently for in vivo studies for multimodality imaging tumor imaging through computed tomography and photoacoustic imaging, and effective cancer treatment combining both photothermal therapy and radiation therapy.^[30] WO_3 and WO_2 transparency can be tuned by inducing a difference of electric potential or electric current, which can enhance or reduce the plasmonic generation of an external Au shell. However, Au and WO_3 are not easily bound

together, therefore an intermediate interface that helps to bind both the Au NPs and the WO_3 core is needed. This intermediate layer needs to have low cytotoxicity for the human cells and should be able to accommodate the Au NPs easily. Porous silica (SiO_2) NPs have previously been utilized to accommodate Au and have shown very low toxicity in the human body.^[31] The synthetic steps are displayed in Figure S1 (Supporting Information). To validate this design (Figure 1a), we will use the well-established Raman reporter on Au, 4-mercaptobenzoic acid (4-MBA), to acquire the SERS signals. The schematic of the SERS process in the Au shell surface is explained in Figure 1b. It also shows that 785 and 830 nm are the two wavelengths used to obtain the Raman signals and maps, which are in the near-infrared region of the electromagnetic spectra. These wavelengths allow human tissue penetration while standard SERS that uses visible light would be fully absorbed by the organic tissues.

2. Results and Discussion

2.1. Characterization of Au– SiO_2 – WO_3 Nanocomposites

Figure 2a displays the X-ray powder diffraction (XRD) patterns of the nanoparticles from each synthesis step. The peaks in each XRD pattern reveal the crystal structure of these materials. Along with the progression, the original monoclinic WO_3 (Blue line) peaks are accompanied with lumps of the amorphous SiO_2 at 23.1° (002), 23.6° (020), and 24.4° (200) (Black line), and then the cubic Au peaks appear (Red line) in the composite, benchmarked against the plain Au NPs at 38.1° (111) and 44.3° (200) (Green line). The three main fingerprint peaks of monoclinic WO_3 at 23.1° , 23.6° , and 24.4° are always present. This result confirms the bulk composite phase structures.

The phases identified by XRD are also verified by high-resolution transmission electron microscopy (HRTEM) imaging. The lattice spacing is 0.265 nm (Figure 2b) for the monoclinic WO_3 (020) core, and 0.235 nm for the Au (111) on top of the intermediate SiO_2 shell (Figure 2b,c). Figure 2d–r shows the scanning transmission electron microscopy (STEM) images of the composite nanoparticles and their corresponding energy-dispersive X-ray spectroscopy (EDX) elemental mapping results. These maps reveal the detailed distribution features of each element at the nanoscale. Figure 2n–r represents the first step of the synthesis and shows that the core contains W and O, while the first shell being Si and O. This is consistent with the expected WO_3 wrapped by SiO_2 . Figure 2i–m is the Au seeding step, in which Au in green color is found surrounding the SiO_2 shell with a homogeneous distribution of small Au seeds. Figure 2d–h demonstrates the thick Au shell growth in green color as compared with that shown previously for the attached Au nanoseeds. Finally, the STEM-EDX and HRTEM results both confirm an average diameter of 3.5 ± 1.0 nm for the particulate Au nanoseeds.

The WO_3 core used in this material is polydispersed and add a big uncertainty in the final shape and size, especially for thin layers of SiO_2 and Au. Also, the purity of the source can

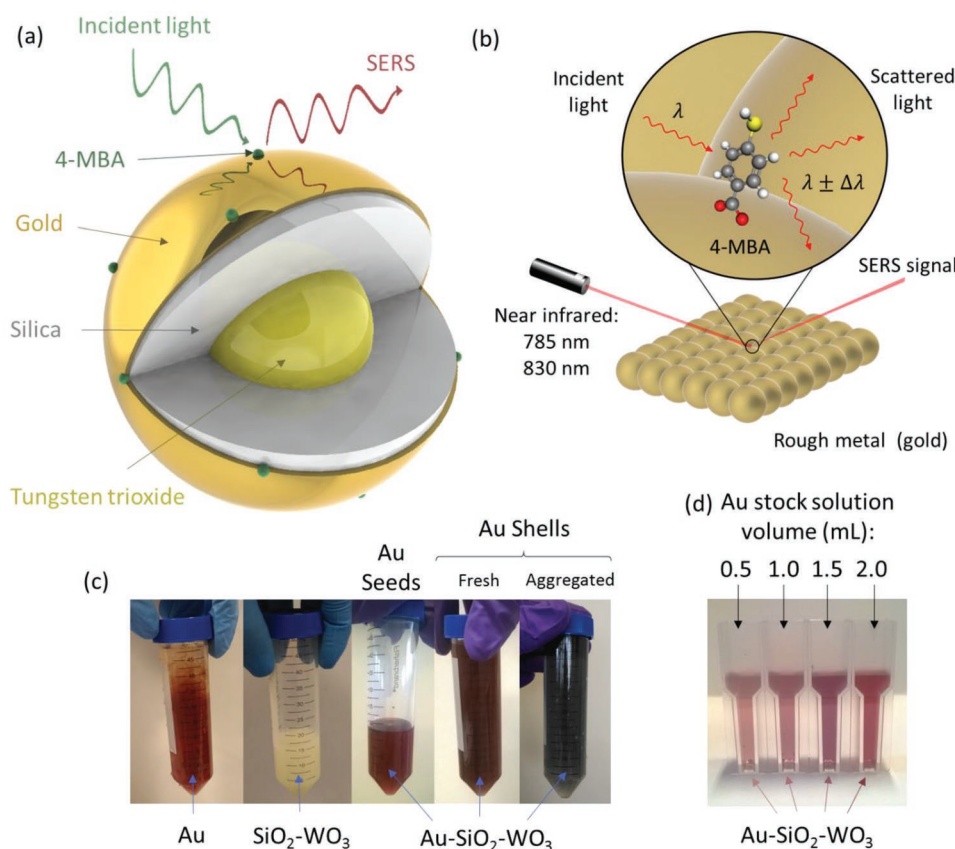


Figure 1. a,b) Schematic of the composite NP design and SERS effect over the gold nanoshell, respectively. c) Colloidal nanoparticles solutions made of Au, $\text{SiO}_2\text{-WO}_3$, and $\text{Au-SiO}_2\text{-WO}_3$ covered with Au seeds and Au shells within thick layers, respectively. d) $\text{Au-SiO}_2\text{-WO}_3$ nanoparticles solutions with various Au thickness obtained by using different Au stock solution during the shell formation.

be refined to avoid crosslinked WO_2 contamination or use WO_2 cores directly during the synthesis, which has smaller energy bandgap for displaying electrochromic behavior. The reduction of the final overall size can help to improve excretion rates of the nanoparticles after imaging.^[32–35]

2.2. Control of SiO_2 Shell Thickness

Figure 3 shows the SiO_2 thickness dependency on the ratio of ammonia:TEOS. To achieve thickness control, the volume of ammonia remains constant at 1 mL for all the displayed coatings in Figure 3. This follows the principles of the Stöber process that describes the growth of SiO_2 NPs.^[36] When the amount of TEOS increases over the ammonia, the coating is thicker, and vice versa (Figure 3a–f). This has been previously addressed using different cores by several authors.^[37–39] The thickness of the SiO_2 can be minimized down to 3 nm. However, the relationship between the thickness and the concentration of TEOS is nonlinear. On the other hand, the current core has been found to exhibit some potential cytotoxicity for certain cells,^[40–42] so it needs to be wrapped thick enough to ensure it never directly interacts with healthy cells. TEOS is the main parameter determining the SiO_2 layer thickness.

2.3. Attachment of Au NPs

There are several very important optical and chemical properties of Au NPs that depend strictly on the type of ligand and ligand-metal bond. 3-Aminopropyltrimethoxysilane (APTS) is one of the most common chemicals used to amine-functionalized surfaces for successive Au attachment due to its stable bonding with Au, fast attachment, and low cost.

Figure 4a displays the sample prepared with 4 times fewer APTS concentration than the one used to prepare the sample shown in Figure 4b during the amine functionalization process. Figure 4 shows that an increment of the APTS content leads to a more homogeneous Au seeding over the SiO_2 surface. The concentration of APTS used in this study produced Au NPs of $3.5 \text{ nm} \pm 1.0 \text{ nm}$ in diameter.

2.4. Plasmonic Light Absorption

Figure 5a shows the ultraviolet–visible (UV–vis) absorption spectra of various synthesis stages, which reveals the plasmon excitation wavelengths and the maximum absorption peak of Au, and the visible color displayed by the colloidal. The plain Au colloidal appears as red, with maximum absorption

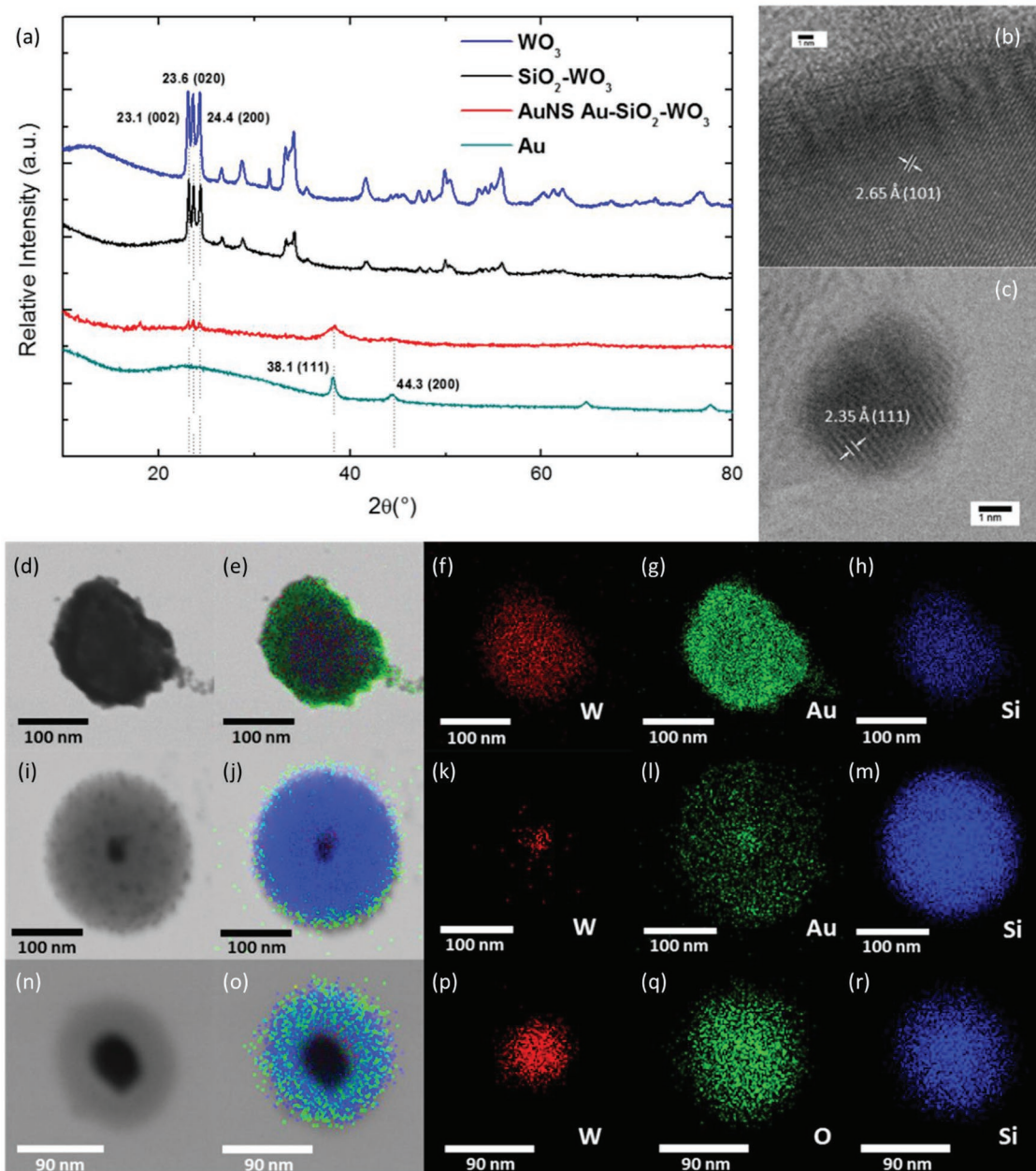


Figure 2. Characterization of the nanocomposites. a) XRD profiles of the WO₃, SiO₂-WO₃, Au-SiO₂-WO₃ and Au. b) HRTEM images of WO₃ and c) Au. d–h) STEM-EDX element mapping of Au nanoshell on Au-SiO₂-WO₃: STEM image, RGB overall, W, Au, and Si, respectively. i–m) STEM-EDX element mapping of Au nanoseeds on Au-SiO₂-WO₃: STEM image, RGB overall, W, Au, and Si, respectively. n–r) STEM-EDX element mapping of SiO₂-WO₃: STEM image, RGB overall, W, O, and Si, respectively.

at 510 nm; whilst the colloidal of nanoshell version of Au-SiO₂-WO₃ appears purple with an absorption peak at 532 nm.^[43] Figure 5b, which corresponds to the colloidal nanoparticles displayed in Figure 1d, displays the evolution of the absorption spectra during the nanoshell formation in which X represents the volume of 25×10^{-3} M Au stock solution as explained in the methods section. Also, there is a clear redshift when the aggregation of the Au and Au-SiO₂-WO₃ NPs takes place. The optimal scenario is a maximum peak in the near-infrared regime to have the highest plasmonic oscillations for the SERS application with

near-infrared laser illumination. There are no local maximum peaks for the nonmetallic materials, as expected since they do not have plasmon resonances. Also, the contribution of SiO₂ is negligible but starts to be relevant for increased wavelengths.

2.5. SERS Maps with 4-MBA Reporter

Figure 6a–c shows the Raman spectra of 4-MBA molecules bound to the shelled Au-SiO₂-WO₃, seeded Au-SiO₂-WO₃ and

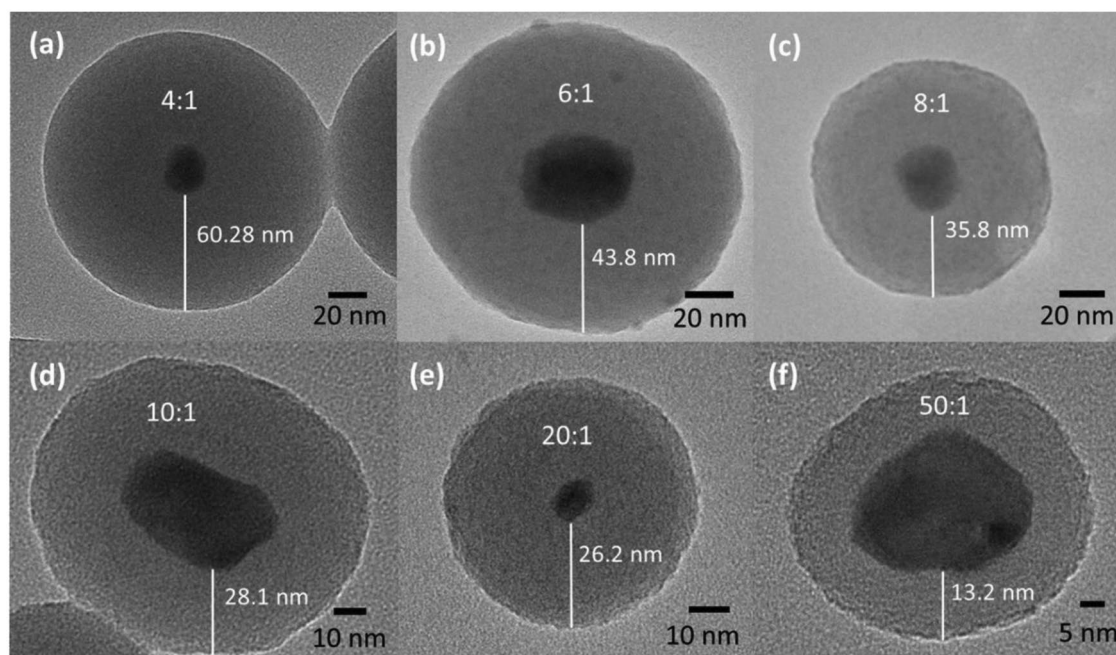


Figure 3. TEM images of $\text{SiO}_2\text{-WO}_3$ samples with different ratios of ammonia:TEOS. a) 4:1, b) 6:1, c) 8:1, d) 10:1, e) 20:1, and f) 50:1.

4-MBA alone, respectively. The substrate that holds the samples is a Si wafer and acts as a reference to control the intensity performance of the vibrational resonance peaks from the fixed concentration and volume of 4-MBA molecules, and therefore, the SERS effect quality. It is clear from Figure 6a–c that for Au content there is a boost in these peaks against the 4-MBA molecule alone in Figure 6c.^[44] The maximum enhancement of 771 times over the original signal is achieved for the core-shell NPs nanoshelled with Au twice as shown in Figure S2b (Supporting Information). This factor is more than four times achieved value with the 3.5 nm Au nanoseeds on the SiO_2 surface from Figure 6b. This implies that for higher resolution and detection power, the complete nanoshell is essential. All the enhancement factor calculations have been carried out using the same Raman reporter molecule concentrations. A quick comparison with previous results using bare Au nanoparticles for the

same overall size shows that these composite nanoparticles achieved lower enhancement factors, mainly due to the bluer maximum absorption peak position.^[45,46] Smaller monodispersed cores and thinner silica shells can be the key for a substantial improvement to match the surface plasmon resonance wavelength. Larger enhancements can be easily achieved by increasing the gold nanoshell thickness while keeping non-smooth surfaces. It can also be improved with the addition of another external Au layer on top of the Raman molecules to create hot spots.

4-MBA is a thiol that contains a benzene ring in the R part, which forms the aromatic ring. This ring provides a strong Raman scattering cross-section with characteristics peaks of 1078 cm^{-1} and 1589 cm^{-1} (see Figure 6). We chose this molecule due to its features of stable sulfur bond with Au, easy attachment, and pH sensitivity in the Raman spectra.^[47]

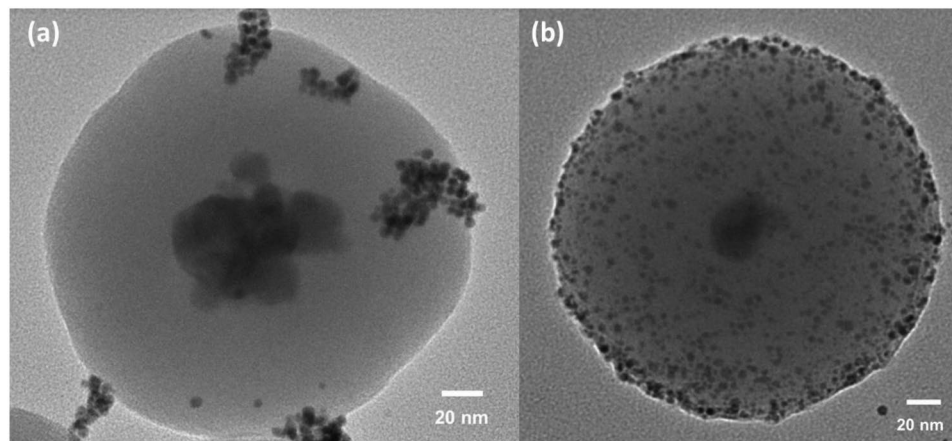


Figure 4. TEM images of Au nanoseeds attachment. Au- $\text{SiO}_2\text{-WO}_3$ NPs synthesized with different APTS additions: a) 50 μL . b) 200 μL .

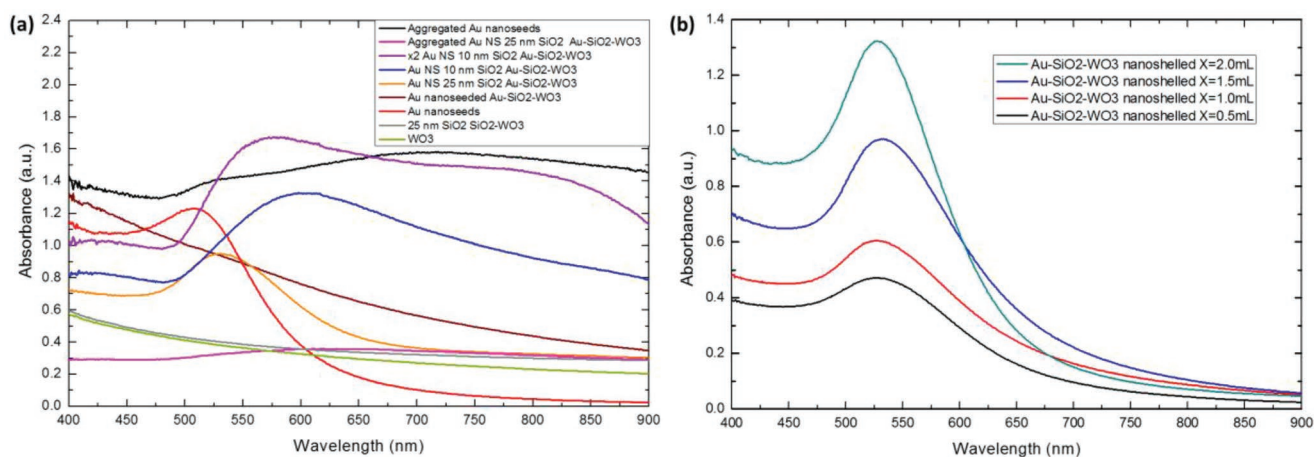


Figure 5. UV-vis absorption spectra of various colloidal nanoparticles: a) WO_3 , $\text{SiO}_2\text{-WO}_3$, Au seeded Au- $\text{SiO}_2\text{-WO}_3$, Au shelled Au- $\text{SiO}_2\text{-WO}_3$ (and aggregated batch, after 2 weeks stored in room temperature) and Au alone (and aggregated batch, after 2 weeks stored in room temperature). b) Au- $\text{SiO}_2\text{-WO}_3$ shelled with different Au stock solution (X) used during the shell formation.

Depending on the intensity and position of the peaks, different thiolated reporter molecules can be investigated to find the most suitable Raman reporters for potential use when labeling specific cell types such as cancer cells. The nanoparticles synthesized in this paper achieve easily improvable 10^4 and 10^3 SERS EFs for one Au shell and double Au shell, respectively, in dried samples over Si wafers (see Figure 6a and Figure S2b, Supporting Information). Also, several orders of magnitude were found for the double Au layer for liquid samples (see Figure S2a, Supporting Information), which is very promising for future in vivo applications due to including optical absorption similar to organic human soft tissue. All these values were obtained by dividing the SERS signal by the background silicon peak to normalize them and subsequently

measuring the ratio of the SERS peak versus the molecule without plasmonic enhancement. Moreover, we have not displayed the Raman enhancement from the Au seeds without attaching to the silica shell because the intensity of the 4-MBA peaks was as strong as the molecules alone for both near-infrared lasers.

Principal component analysis (PCA) is an adaptive data analysis technique that combines conventional imaging and spectroscopy to simultaneously obtain both spatial and spectral information from an object by reducing a large set of possibly correlated variables to a small set of uncorrelated variables, called principal components that still contains most of the relevant information from the large set.^[48,49] The origin of the new coordinate system is located in the center

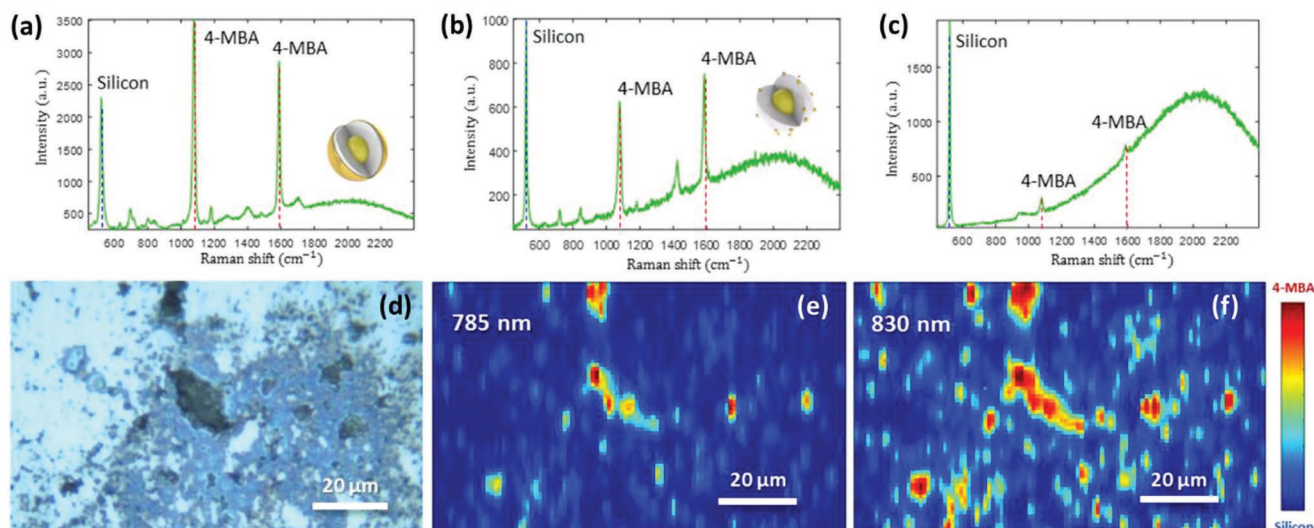


Figure 6. a–c) SERS spectra of 4-MBA molecule peaks at 1078 and 1589 cm^{-1} with 830 nm laser and d–f) Raman maps with 785 and 830 nm of different samples with 4-MBA Raman reporter over a silicon wafer with its characteristic reference peak at 520 cm^{-1} . a) Au shelled Au- $\text{SiO}_2\text{-WO}_3$. b) Au seeded Au- $\text{SiO}_2\text{-WO}_3$. c) Plain 4-MBA molecules. d–f) Optical microscopy image, Raman maps under PC1 (66.09%) taken with 785 nm and 830 nm lasers, respectively.

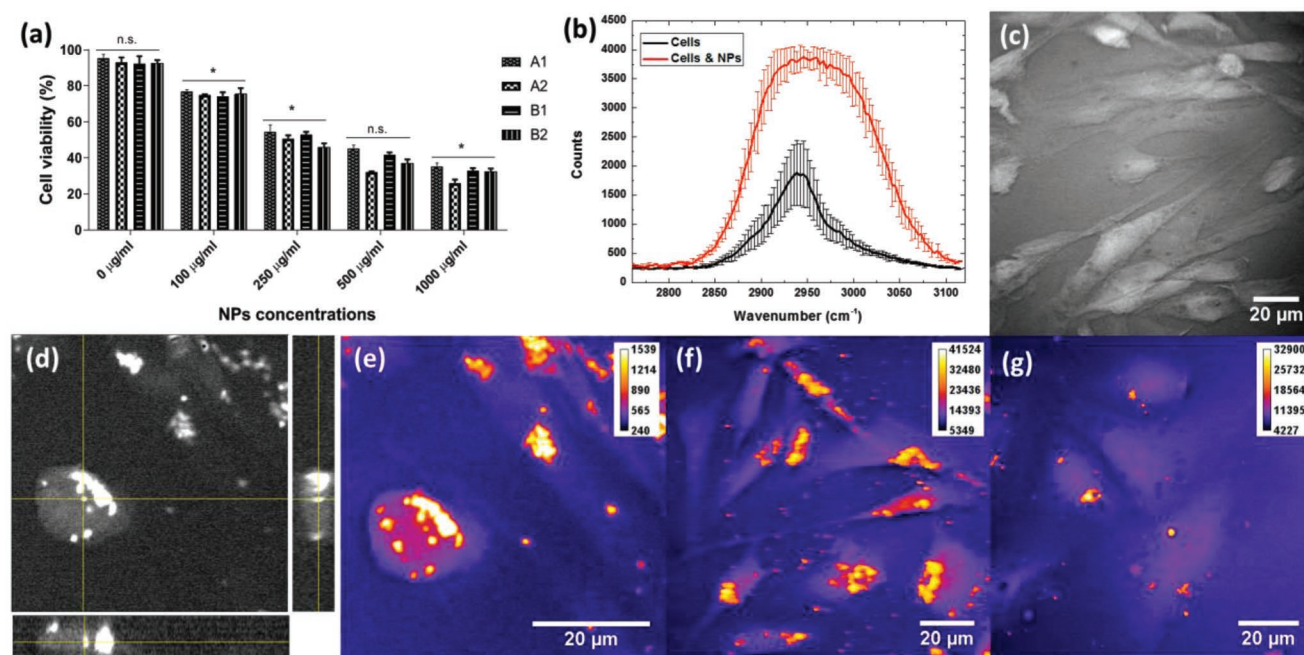


Figure 7. a) Cytotoxicity tests after 24 h of samples A1 (single layer of Au), A2 (single layer of Au coated with 4MBA), B1 (double layer of Au) and B2 (double layer of Au coated with 4MBA). The values represent the mean \pm standard deviation of three experiments; * denotes $p < 0.05$ (statistical significance) and ns represents $p \geq 0.05$ (nonstatistical significance). b) Average values and standard deviations errors from CARS spectra from cells alone and cells with nanoparticles. c) Control cells CARS stack—z-projection image in grayscale. d) CARS 3D demonstration of nanoparticles B1 within the cell in grayscale and e) its z-projection of the entire stack (recolored intensity-dependent with fire LUT in ImageJ). f) Nanoparticles A2 in cells CARS imaging (recolored intensity-dependent with fire LUT in ImageJ). g) z-stacking of CARS images from cells and nanoparticles stack A1 (recolored intensity-dependent with fire LUT in ImageJ).

of the data points, the first PCA step includes the points in the direction of the highest variance, the second PCA step includes the ones for the second-highest variance and the rest follow this trend. Using the first PCA, which describes the greatest variance in the dataset (66.09%) in the Raman maps, we can find where the 4-MBA molecules are located: dark red means 4-MBA and dark blue represents the Si wafer (Figure 6e,f). This information is not obvious from the optical image (Figure 6d); however, the Raman maps are able to identify the locations of these reporters. The SERS intensity of the aggregated areas is not only due to the 2D spatial distribution of the materials but also due to having several layers that lead to stronger hot spots^[50] and cannot be seen with the optical microscope. After subsequent attachment of the nanoparticles to or uptake into cancer cells, the cancer cells will be precisely located.

Targeting and localization of cancer cells can be achieved by functionalizing the Au nanoshell with cancer ligands such as antibodies, which are customized for each type of cancer. One type of promising ligand is the anti-HER monoclonal antibodies for the treatment of various types of cancers including HER-2⁺ metastatic breast, colorectal, NSCLC, pancreatic, breast, HNSCC, ovarian and renal tumors.^[51,52] Should these core-shell nanoparticles provide sufficient signals in combination with bright Raman reporters in the near-infrared, the SERS signals could be readout using microscopy in individual cancer cells. Moreover, they also could visualize in vivo tissues with Raman fiber probes or surface-enhanced spatially offset Raman spectroscopy (SESORS).

2.6. Cytotoxicity Profile in a Triple-Negative Human Breast Cancer Cell Line MDA-MB 231

Figure 7a shows the in vitro cytotoxicity profile of the selected concentrations (100, 250, 500, and 1000 $\mu\text{g mL}^{-1}$) of four different batches (A1, A2, B1, B2) of Au-SiO₂-WO₃ nanoparticles in a triple-negative human breast cancer cell line MDA-MB 231. A1, A2, B1, B2 represent single layer of Au, single layer of Au coated with 4MBA, double layer of Au and double layer of Au coated with 4MBA, respectively. The NPs concentration range was selected from the minimum concentration showing low toxicity to concentration showing maximum toxicity. A live-dead assay for a period of 24 h was performed to confirm the suitability of the nanoparticles for biomedical applications. Statistical analysis was performed with three batches per sample and concentration of which the mean and standard deviation were calculated. The results show no statistical significance (ns, $p \geq 0.05$) for concentrations 500 $\mu\text{g mL}^{-1}$, while for concentrations of 100, 250, and 1000 $\mu\text{g mL}^{-1}$ the results are statistically significant (*, $p < 0.01$ to 0.05) as shown in Figure 7a. Among the statistically significant results, low cytotoxicity (>75% alive cells) after 24 h was found for concentrations of 100 $\mu\text{g mL}^{-1}$ indicating their suitability for cell imaging purposes.

2.7. Cell Imaging in Human MDA-MB 231 Breast Cancer Cells

The cancer cells were visualized by imaging the CARS signal generated from the CH molecular vibrations within the

cells, this signal was chemically specific with a peak around 2940 cm^{-1} . The nanoparticles within the cells also exhibited a very strong signal within the CARS channel, however, this was from a four-wave mixing process, which was not chemically specific. Figure 7b compares the spectra of the cells to the spectral of the Au-SiO₂-WO₃ NPs within the cells. The average value and standard deviation of three measurements were taken and plotted for both the cells only and the cells with the NPs. The intensity of the signal in cells with NPs is a few times higher than cells alone, which indicates high sensitivity to locate the NPs. Figure 7c–g shows the cell imaging results obtained with CARS. The control label-free human MDA-MB 231 breast cancer cells without nanoparticles are shown in Figure 7c, this image is a z-projection of a CARS image stack and the contrast is from the CH vibrations within the cells. Then, in Figure 7d, CARS 3D cross-sections of NPs with a double layer of Au (white color) within the cells (gray color) in gray confirms that the nanoparticles were uptaken by the cells and can be seen from the inside of the cells. Additionally, the z-projection of the entire stack of CARS images was implemented in Figure 7e by applying the color filter fire look-up-tables (LUT) in ImageJ over the original intensity-dependent greyscale. This recolored image shows the nanoparticles (white) located inside the cells (purple) at different z-positions. Similarly, Figure 7f,d shows the z-projection of the entire stack with fire LUT recoloration for nanoparticles with a single layer of Au coated with 4MBA and without 4MBA, respectively. These results along with the cytotoxicity profiles confirm the viability for these nanoparticles to be used in cancer cell imaging.

3. Conclusion

In summary, we have demonstrated a size tunable synthesis method to obtain novel Au-SiO₂-WO₃ NPs. Higher APTS concentrations result in attachment of larger numbers of seeding Au NPs over the SiO₂ layer. Along with the synthesis, modifications in the intensity of the ultrasonication and speed in the centrifugation can be introduced to refine the washing process and avoid nanoparticles agglomerations. On the one hand, by repeating the Au shell growth step, several gold shells are created and stronger SERS is achieved as displayed in Figure S2a (Supporting Information). This ability to increase the enhancement factor is crucial for translational biomedical applications that involve media that attenuates the near-infrared laser intensity. On the other hand, the main parameter for the SiO₂ thickness growth is the ratio between TEOS and ammonia. Higher ratios of ammonia:TEOS lead to thinner SiO₂ thickness, which reduces the potential toxicity in the human body through a faster excretion. However, it could increase the risk of displaying cytotoxicity related to partially uncoated WO₃ cores. The final Au-SiO₂-WO₃ NPs have been systematically obtained in more than 10 batches by following the synthetic procedure, this reflects the high reproducibility of the synthesis. The optimal thickness of the SiO₂ and Au nanoshells for both strong SERS and low toxicity has yet to be determined. However, preliminary results from various configurations show highly reproducible accurate nanoparticles detection in 2D human breast cancer cell culture and liquid media which leads to believe in vivo cell

imaging can be achieved. Moreover, cytotoxicity tests after 24 h show >75% alive cells from statistically significant cell viability at concentrations of $100\text{ }\mu\text{g mL}^{-1}$. This is a very promising translational result that encourages the use of these nanoparticles in future live human cancer cells imaging and 3D human cell culture models such as spheroids, organoids and organ-on-a-chip technologies to have the full picture of how beneficial these nanoparticles can be in the clinical stage.

4. Experimental Section

Materials: All the following reagents were purchased from Sigma-Aldrich: gold(III) chloride hydrate (HAuCl₄·xH₂O, 99.999% trace metals basis M_w 339.79 g mol⁻¹), tetrakis (hydroxymethyl)phosphonium chloride solution (THPC, 80% in H₂O), (3-aminopropyl)triethoxysilane (APTS), potassium carbonate (K₂CO₃, 99.995% trace metals basis M_w 138.21 g mol⁻¹), sodium hydroxide (NaOH, Sigma-Aldrich), potassium carbonate (K₂CO₃), formaldehyde (CH₂O (H-CHO)), 4-mercaptobenzoic acid (MBA), deionized water, ethanol, formaldehyde solution, Dulbecco's modified Eagle's medium (DMEM), trypsin-EDTA solution, and cell proliferation reagent WST-1. The WO₃ nanoparticles were purchased from China, Chang Sha Na Ro Mei Nanomaterials Ltd, with a purity of 99.9% and an average size of 40 nm. Culture cell serum-supplement and penicillin-streptomycin were purchased from Gibco.

Cell Culture: The MDA-MB 231 human breast cancer cells were cultured in DMEM with 10% serum-supplement and 1% penicillin-streptomycin. Cells were grown under standard conditions of 5% CO₂ and 37°C in a controlled humidified incubator to reach 70–80% confluence. Cells were routinely subcultured using 0.25% trypsin-EDTA solution.

Characterization Instruments and Conditions: The nanoparticles were characterized by using the Thermo Scientific Evolution Array UV-vis spectrophotometer to obtain the light absorption spectra of the colloidal composite nanoparticles suspended in ethanol at mild conditions. For the electron microscopy images and the EDX element maps, the JEOL 2100 TEM/STEM system was used. The XRD patterns were obtained with the Bruker D8 advanced XRD machine working at 0.03° step per second of 2θ from 10° to 80° at room temperature. Raman signals, maps, and optical images for dried samples were obtained from samples dried on top of silicon wafers by using 785 and 830 nm lasers integrated into the Renishaw Invia Raman system and with its internal optical microscope at standard room conditions.

Silica Nanoshell Formation: The first step was the synthesis of the SiO₂-WO₃ core-shell nanocomposites (Figure S1, Supporting Information), NP following the Stober process. A liquid suspension made of 10 mL deionized (DI) water, 20 mL ethanol, and 0.015 g WO₃ NPs was first prepared, then a modified Stober process promoted the formation of the SiO₂ shell via the sol-gel method. In this method, consecutive hydrolysis and condensation of alkoxysilanes in an aqueous-alcoholic solution in the presence of a base catalyst were involved, using tetraethyl orthosilicate (TEOS) as alkoxysilane and ammonia as the base catalyst.

In this paper, a different route from other Stober-based versions was taken to perform the silica synthesis while in parallel coating the core. WO₃ NPs were coated with SiO₂ by adding 1 mL ammonia and 5 drops of TEOS while stirring the WO₃ suspension with a time interval of 10 s between each TEOS drop. This was the key to create the SiO₂ coating because by changing the concentration of TEOS the SiO₂ thickness could be modified. After that, the mixture was stirred continuously for 30 more min. The ammonia concentration catalyzed this reaction by increasing the reaction rate. Finally, the suspension was washed with deionized water and Ethanol by centrifugation to separate the nanoparticles from the liquid in 50 mL Eppendorf tubes.

Amine Functionalization: The SiO₂-WO₃ core-shell nanocomposite surfaces were functionalized with an amine group. First, 0.015 g

SiO₂-WO₃ core-shell nanocomposites (Figure S1, Supporting Information) was dispersed in 20 mL of ethanol in a beaker and subjected to 30 min ultrasonic probe treatment. Then, 500 μ L of APTS was added to the suspension, which was heated to 70 °C under the magnetic stirring for 5 h. To remove the excess reactants, the suspension of 25 mL ethanol was centrifuged for three times (10 min per cycle at 6 000 rpm) without washing and redispersed by ultrasonic probe treatment.

The key aspect of this functionalization was the NH₂ ending on top.^[53] These NH₂ ligands reacted with Au after breaking it in two parts by heating. On the one hand, H₂ was released on one side when the H atoms absorbed higher energy than the bond. On the other hand, a very strong bond was created between the N and the Au atoms that were close enough to be attracted by the electric force of the N²⁻ ions and the Au electron cloud. This fact made it possible to attach Au nanoseeds and to stable subsequent Au growth on top with homogeneous distribution.

Colloidal Au-SiO₂-WO₃ NPs Fabrication: Colloidal Au NPs can be obtained following different methods, which are based on the work of Turkevich et al.^[54] Herein they were NP obtained by reducing Au salts (HAuCl₄) in the presence of surfactants, tetrakis (hydroxymethyl) phosphonium chloride (THPC, C₄H₁₂ClO₄P).^[55] During the formation of the metallic solution, a huge excess of NaOH was formed. The reactions between THPC and NaOH produced formaldehyde as the reducing agent for Au. After the amine functionalization, the gold coating process is implemented.

By dissolving 0.098 g of HAuCl₄·3H₂O in 10 mL of deionized water, a 25.0 $\times 10^{-3}$ M Au stock solution was prepared, called chloroauric acid. By typical reducing the chloroauric acid with THPC, the colloidal Au NPs (13 $\times 10^{-9}$ M) was prepared. In detail, 3 mL of 1 M NaOH (0.2 g in 5 mL deionized water) and 1 mL of diluted THPC (12 μ L of 80% THPC per 1 mL of deionized water, 50 $\times 10^{-3}$ M) were added to 44 mL of deionized water while being stirred. The solution was magnetically stirred for 5 min and 2 mL of the 25 $\times 10^{-3}$ M Au stock solution was rapidly added in and the color quickly changed to dark red or brown. The final Au colloidal was stored at 5 °C for 12 h, prior to being used for later Au coating process.

5 mL of the amine-functionalized SiO₂ core-shell nanocomposites suspension of 70 °C was added to 20 mL of magnetically stirred Au colloidal NP of 100 °C, and then continuously stirred for 10 min. The resulting colloidal suspension NP was washed with deionized water under centrifugation for three times at 6000 rpm for 10 min each time, to remove the excess of reactants.

Au Shell Synthesis: Once the Au nanoseeds were attached to the SiO₂ nanoshell, the Au started to grow to form the final out layer.^[56] The alkaline growth solution was prepared by dissolving 0.025 g potassium carbonate (K₂CO₃) in 100 mL deionized water (0.18 $\times 10^{-3}$ M). Then 1.5 mL of 25 $\times 10^{-3}$ M (1% w/v) of the Au stock solution was added to the growth solution, and the mixture was stirred until the yellow colloidal suspension became clear (transparent). 20 mL of this clear solution was injected with 1 mL of the Au-SiO₂-WO₃ NPs suspension, then 100 μ L of formaldehyde was added, and a color change from colorless to purple was observed which is characteristic of the Au nanoshell formation. The resultant suspension was then centrifuged and redispersed in water, for later UV-vis spectrophotometry and Raman spectroscopy characterization.

Adding Reporter Molecule for SERS: The Au nanoshell bioconjugation was achieved by mixing 4-mercaptobenzoic acid (4-MBA) diluted in ethanol with the Au-SiO₂-WO₃ nanocomposites.^[57] After these synthesis steps, thiolated Au-SiO₂-WO₃ core-shell nanocomposites were obtained. Figure S1 (Supporting Information) describes the entire synthesis steps. 1 $\times 10^{-3}$ M of 4-MBA solution was prepared by diluting an appropriate mass of the solid in ethanol (or aqueous). For the collection of SERS spectra, 100 μ L of 1 $\times 10^{-3}$ M solution of 4-MBA was mixed with 1 mL of colloidal Au NPs. After 5 min stirring, the mixture was centrifuged three times for 7 min at 4000 rpm in 1.5 mL Eppendorf tubes, and the supernatant was redissolved in deionized water.

Cell Viability: Cell viability experiments were performed in 96-well plates and imaging experiments were performed in six-well plate. Cells were seeded in a 96-well plate at the density of 1 $\times 10^4$ cells per well

while cells were seeded onto the six-well plates at a density of 1 $\times 10^6$ cells per well and incubated for 24 h prior to the experiments. After overnight incubation, cells were treated with and without 100, 250, 500, and 1000 μ g mL⁻¹ of four types of NPs for 24 h. Cell viability after nanoparticle treatment was determined using WST-1 assay (Roche Applied Biosystems) according to the manufacturer's instructions with modifications to adapt for nanoparticle-treated cells. Briefly, cells were seeded in a 96-well plate with a density of 1 $\times 10^4$ cells per well, differentiated and incubated with nanoparticles (three replicates per concentration). After 24 h, WST-1 reagent was added to the cells, and after the color reaction, the plate was then kept for shaking and then absorbance was measured at a wavelength of 450 nm using a plate reader (Clariostar plate reader, BMG labtech). The results were expressed as percentage cell viability. Three independent experiments were performed for each study and all measurements were performed in triplicate.

Statistical Analysis: The data were statistically analyzed using GraphPad Prism 5.04 to assess the effects of NPs treatment on cell viability and were expressed as % cell count \pm SD, Mann Whitney. * ($p < 0.05$) was considered statistically significant. Results were presented as the mean \pm standard deviation (SD).

Cell Imaging Using Coherent Antistokes Raman Spectroscopy: Coherent anti-Stokes Raman scattering (CARS) imaging was carried by using dual-wavelength output from an InSight X3 ultrafast fs laser (Newport SpectraPhysics) with 800 nm for the pump and probe beam and 1045 nm as the Stokes beam. The beams were chirped to produced ps pulses and spatially overlaid in the Spectral Focusing Timing and Recombination Unit (SF-TRU, Newport SpectraPhysics). The temporal overlap between the pump and Stokes beams was scanned via the SF-TRU unit to allowing us to rapidly change which Raman vibration was probed, and acquire spectral data.^[58] 3D submicron resolution imaging was performed on a modified confocal microscope (Olympus FV3000), with a 60 \times water-immersion objective (1.2NA, UPlanSApo, Olympus). The anti-Stokes light at 648 nm from CARS was collected in the forward direction using a water immersion objective (Olympus LUMPlanFLN 60X). The anti-Stokes light was separated from the laser fundamentals by using a long pass dichroic beamsplitter (Chroma DC/T760lpxr) followed by two filters (Chroma ET650/45x) and detected using a PMT (Hamamatsu R3896). The samples were mounted between two coverslips. To avoid photodamage to the samples, the laser intensities were attenuated to give 9 and 18 mW for the pump and Stokes beams in the sample plane, respectively.

Supporting Information

Supporting Information is available from the Wiley Online Library or from the author.

Acknowledgements

P.M.P., K.T., and Y.Z. designed the nanocomposites. P.M.P. and H.C. characterized the nanocomposites. P.M.P., L.C., and N.S. designed the 4-MBA functionalization. P.M.P. and L.C. measured the Raman maps on silicon wafers and the SERS effect. B.G. and P.M.P. obtained the nanoparticles SERS Raman spectra in liquid samples. T.A.T. and P.M.P. designed and performed the cytotoxicity studies. J.M., P.M.P., and T.A.T. designed and carried out the cell imaging. P.M.P. drafted the manuscript, and all co-authors contributed to modification. P.M.P., Y.Z., and N.S. led the project. Thank Ellen Green and Pascaline Bouzy for technical supports in Raman measurements. The authors acknowledge Professor Julian Moger for providing access to the CONTRAST facility for the CARS imaging (this facility was funded by the Engineering and Physical Sciences Research Council (EPSRC) grant number (EP/5009957/1). P.M.P. acknowledge financial support from the EPSRC of the United Kingdom, via the EPSRC Centre for Doctoral Training in Metamaterials (Grant No. EP/L015331/1). All data created during this research are openly available from the University of Exeter's institutional repository.

Conflict of Interest

The authors declare no conflict of interest.

Keywords

cancer imaging, core-shell, gold, SERS, tungsten oxide

Received: May 3, 2019

Revised: August 14, 2019

Published online: September 9, 2019

- [1] M. D. Farwell, D. A. Pryma, D. A. Mankoff, *Cancer* **2014**, 120, 3433.
- [2] D. I. Ellis, D. P. Cowcher, L. Ashton, S. O'Hagan, R. Goodacre, *Analyst* **2013**, 138, 3871.
- [3] J. P. B. O'Connor, E. O. Aboagye, J. E. Adams, H. J. W. L. Aerts, S. F. Barrington, A. J. Beer, R. Boellaard, S. E. Bohndiek, M. Brady, G. Brown, D. L. Buckley, T. L. Chenevert, L. P. Clarke, S. Collette, G. J. Cook, N. M. deSouza, J. C. Dickson, C. Dive, J. L. Evelhoch, C. Faivre-Finn, F. A. Gallagher, F. J. Gilbert, R. J. Gillies, V. Goh, J. R. Griffiths, A. M. Groves, S. Halligan, A. L. Harris, D. J. Hawkes, O. S. Hoekstra, E. P. Huang, B. F. Hutton, E. F. Jackson, G. C. Jayson, A. Jones, D.-M. Koh, D. Lacombe, P. Lambin, N. Lassau, M. O. Leach, T.-Y. Lee, E. L. Leen, J. S. Lewis, Y. Liu, M. F. Lythgoe, P. Manoharan, R. J. Maxwell, K. A. Miles, B. Morgan, S. Morris, T. Ng, A. R. Padhani, G. J. M. Parker, M. Partridge, A. P. Pathak, A. C. Peet, S. Punwani, A. R. Reynolds, S. P. Robinson, L. K. Shankar, R. A. Sharma, D. Soloviev, S. Stroobants, D. C. Sullivan, S. A. Taylor, P. S. Tofts, G. M. Tozer, M. van Herk, S. Walker-Samuel, J. Wason, K. J. Williams, P. Workman, T. E. Yankeelov, K. M. Brindle, L. M. McShane, A. Jackson, J. C. Waterton, *Nat. Rev. Clin. Oncol.* **2016**, 14, 169.
- [4] A. C. Anselmo, S. Mitragotri, *Bioeng. Transl. Med.* **2016**, 1, 10.
- [5] K. Ma, H. Sai, U. Wiesner, *J. Am. Chem. Soc.* **2012**, 134, 13180.
- [6] F.-Y. Cheng, C.-T. Chen, C.-S. Yeh, *Nanotechnology* **2009**, 20, 425104.
- [7] K. Kan-Dapaah, N. Rahbar, W. Soboyejo, *Med. Phys.* **2015**, 42, 2203.
- [8] J. F. Hainfeld, D. N. Slatkin, T. M. Focella, H. M. Smilowitz, *Br. J. Radiol.* **2006**, 79, 248.
- [9] Z. R. Stephen, F. M. Kievit, M. Zhang, *Mater. Today* **2011**, 14, 330.
- [10] J. Zhao, J. Chen, S. Ma, Q. Liu, L. Huang, X. Chen, K. Lou, W. Wang, *Acta Pharm. Sin. B* **2018**, 8, 320.
- [11] M. Rogosnitzky, S. Branch, *BioMetals* **2016**, 29, 365.
- [12] N. Singh, G. J. S. Jenkins, R. Asadi, S. H. Doak, *Nano Rev.* **2010**, 1, 5358.
- [13] V. Tuchin, *Tissue Optics: Light Scattering Methods and Instruments for Medical Diagnosis*, Vol. PM166, 2nd ed., SPIE Press Book, Bellingham, WA **2007**, p. 882.
- [14] L. Fabris, *J. Opt.* **2015**, 17, 114002.
- [15] D. Gontero, A. V. Veglia, A. G. Bracamonte, D. Boudreau, *RSC Adv.* **2017**, 7, 10252.
- [16] J. H. Kim, P. P. Pompa, H. G. Baek, B. H. Chung, *Nanotechnology* **2016**, 27, 175704.
- [17] S. J. Oldenburg, R. D. Averitt, S. L. Westcott, N. J. Halas, *Chem. Phys. Lett.* **1998**, 288, 243.
- [18] M. Hu, J. Chen, Z.-Y. Li, L. Au, G. V. Hartland, X. Li, M. Marquez, Y. Xia, *Chem. Soc. Rev.* **2006**, 35, 1084.
- [19] Z. Qiao, G. Jianping, G. James, H. Yongxing, S. Yugang, Y. Yadong, *Adv. Mater.* **2010**, 22, 1905.
- [20] R. Ashayer, S. H. Mannan, S. Sajjadi, *Colloids Surf., A* **2008**, 329, 134.
- [21] K. Sokolov, M. Follen, J. Aaron, I. Pavlova, A. Malpica, R. Lotan, R. Richards-Kortum, *Cancer Res.* **2003**, 63, 1999.
- [22] D. Barchiesi, *J. Opt. Soc. Am. A* **2015**, 32, 1544.
- [23] P. J. Vikesland, R. L. Rebodos, J. Y. Bottero, J. Rose, A. Masion, *Environ. Sci. Nano* **2016**, 3, 567.
- [24] E. C. Abenojar, S. Wickramasinghe, J. Bas-Concepcion, A. C. S. Samia, *Prog. Nat. Sci.: Mater. Int.* **2016**, 26, 440.
- [25] S. F. Chen, A. Aldalbahi, P. X. Feng, *Sensors* **2015**, 15, 27035.
- [26] H. Zheng, J. Z. Ou, M. S. Strano, R. B. Kaner, A. Mitchell, K. Kalantar-zadeh, *Adv. Funct. Mater.* **2011**, 21, 2175.
- [27] R. Chatten, A. V. Chadwick, A. Rougier, P. J. D. Lindan, *J. Phys. Chem. B* **2005**, 109, 3146.
- [28] G. Baldissera, C. Persson, *Eur. Phys. J. B* **2013**, 86, 273.
- [29] G. Duan, L. Chen, Z. Jing, P. De Luna, L. Wen, L. Zhang, L. Zhao, J. Xu, Z. Li, Z. Yang, R. Zhou, *Chem. Res. Toxicol.* **2019**, 32, 1357.
- [30] L. Wen, L. Chen, S. Zheng, J. Zeng, G. Duan, Y. Wang, G. Wang, Z. Chai, Z. Li, M. Gao, *Adv. Mater.* **2016**, 28, 5072.
- [31] H. Yang, C. Liu, D. Yang, H. Zhang, Z. Xi, *J. Appl. Toxicol.* **2009**, 29, 69.
- [32] J. Lu, S. Yang, K. M. Ng, C.-H. Su, C.-S. Yeh, Y.-N. Wu, D.-B. Shieh, *Nanotechnology* **2006**, 17, 5812.
- [33] R. Hardman, *Environ. Health Perspect.* **2006**, 114, 165.
- [34] M. Arruebo, R. Fernández-Pacheco, M. R. Ibarra, J. Santamaría, *Nano Today* **2007**, 2, 22.
- [35] M. Longmire, P. L. Choyke, H. Kobayashi, *Nanomedicine* **2008**, 3, 703.
- [36] W. Stöber, A. Fink, E. Bohn, *J. Colloid Interface Sci.* **1968**, 26, 62.
- [37] M. Ohmori, E. Matijević, *J. Colloid Interface Sci.* **1992**, 150, 594.
- [38] A. Guerrero-Martínez, J. Pérez-Juste, L. M. Liz-Marzán, *Adv. Mater.* **2010**, 22, 1182.
- [39] A. Vanderkooy, Y. Chen, F. Gonzaga, M. A. Brook, *ACS Appl. Mater. Interfaces* **2011**, 3, 3942.
- [40] A. M. Yassin, M. Elnouby, N. M. El-Deeb, E. E. Hafez, *Appl. Biochem. Biotechnol.* **2016**, 180, 623.
- [41] Z. Zhou, B. Kong, C. Yu, X. Shi, M. Wang, W. Liu, Y. Sun, Y. Zhang, H. Yang, S. Yang, *Sci. Rep.* **2014**, 4, 3653.
- [42] A. L. Popov, N. M. Zholobak, O. I. Balko, O. B. Balko, A. B. Shcherbakov, N. R. Popova, O. S. Ivanova, A. E. Baranchikov, V. K. Ivanov, *J. Photochem. Photobiol., B* **2018**, 178, 395.
- [43] B. G. Prevo, S. A. Esakoff, A. Mikhailovsky, J. A. Zasadzinski, *Small* **2008**, 4, 1183.
- [44] M. M. Y. Chen, A. Katz, *Langmuir* **2002**, 18, 8566.
- [45] J. D. Driskell, R. J. Lipert, M. D. Porter, *J. Phys. Chem. B* **2006**, 110, 17444.
- [46] H. J. Butler, S. W. Fogarty, J. G. Kerns, P. L. Martin-Hirsch, N. J. Fullwood, F. L. Martin, *Analyst* **2015**, 140, 3090.
- [47] S. Jung, J. Nam, S. Hwang, J. Park, J. Hur, K. Im, N. Park, S. Kim, *Anal. Chem.* **2013**, 85, 7674.
- [48] I. T. Jolliffe, J. Cadima, *Phil. Trans. R. Soc. A* **2016**, 374, 20150202.
- [49] A. A. Gowen, C. P. O'Donnell, M. Taghizadeh, P. J. Cullen, J. M. Frias, G. Downey, *J. Chemom.* **2008**, 22, 259.
- [50] T. Chen, H. Wang, G. Chen, Y. Wang, Y. Feng, W. S. Teo, T. Wu, H. Chen, *ACS Nano* **2010**, 4, 3087.
- [51] F. J. Esteva, *Oncologist* **2004**, 9, 4.
- [52] T. Carter, P. Mulholland, K. Chester, *Immunotherapy* **2016**, 8, 941.
- [53] A. Cossaro, M. Dell'Angela, A. Verdini, M. Puppini, G. Kladnik, M. Coreno, M. de Simone, A. Kivimäki, D. Cvetko, M. Canepa, L. Floreano, *J. Phys. Chem. C* **2010**, 114, 15011.
- [54] J. Turkevich, P. C. Stevenson, J. Hillier, *Discuss. Faraday Soc.* **1951**, 11, 55.
- [55] J. L. Hueso, V. Sebastian, A. Mayoral, L. Uson, M. Arruebo, J. Santamaría, *RSC Adv.* **2013**, 3, 10427.
- [56] M. L. Brongersma, *Nat. Mater.* **2003**, 2, 296.
- [57] A. B. Serrano-Montes, J. Langer, M. Henriksen-Lacey, D. de Aberasturi, D. M. Solís, J. M. Taboada, F. Obelleiro, K. Sentosun, S. Bals, A. Bekdemir, F. Stellacci, L. M. Liz-Marzán, *J. Phys. Chem. C* **2016**, 120, 20860.
- [58] A. Zeytunyan, T. Baldacchini, R. Zadayan, *Proc. SPIE* **2018**, 10498, 104980K-1.